

1

²A SEARCH FOR LONG-LIVED, CHARGED, SUPERSYMMETRIC PARTICLES
³USING IONIZATION WITH THE ATLAS DETECTOR

4

BRADLEY AXEN

5

September 2016 – Version 0.22

6



⁸ Bradley Axen: *A Search for Long-Lived, Charged, Supersymmetric Particles using Ion-
⁹ ization with the ATLAS Detector*, Subtitle, © September 2016

10

Usually a quotation.

11

Dedicated to.

₁₂ ABSTRACT

₁₃ How to write a good abstract:

₁₄ <https://plg.uwaterloo.ca/~migod/research/beck00PSLA.html>

₁₅ PUBLICATIONS

₁₆ Some ideas and figures have appeared previously in the following publications:

₁₇

₁₈ Put your publications from the thesis here. The packages `multibib` or `bibtopic`
₁₉ etc. can be used to handle multiple different bibliographies in your document.

²¹ ACKNOWLEDGEMENTS

²² Put your acknowledgements here.

²³

²⁴ And potentially a second round.

²⁵

26 CONTENTS

27	I	INTRODUCTION	1
28	1	INTRODUCTION	3
29	II	THEORETICAL CONTEXT	5
30	2	STANDARD MODEL	7
31	2.1	Particles	7
32	2.2	Interactions	8
33	2.3	Limitations	8
34	3	SUPERSYMMETRY	9
35	3.1	Motivation	9
36	3.2	Structure	9
37	3.3	Phenomenology	9
38	4	LONG-LIVED PARTICLES	11
39	4.1	Mechanisms	11
40	4.1.1	Examples in Supersymmetry	11
41	4.2	Phenomenology	11
42	4.2.1	Disimilarities to Prompt Decays	11
43	4.2.2	Characteristic Signatures	11
44	III	EXPERIMENTAL STRUCTURE AND RECONSTRUCTION	13
45	5	THE LARGE HADRON COLLIDER	15
46	5.1	Injection Chain	15
47	5.2	Design and Parameters	15
48	5.3	Luminosity	15
49	6	THE ATLAS DETECTOR	17
50	6.1	Coordinate System	17
51	6.2	Magnetic Field	17
52	6.3	Inner Detector	17
53	6.3.1	Pixel Detector	17
54	6.3.2	Semiconductor Tracker	17
55	6.3.3	Transition Radiation Tracker	17
56	6.4	Calorimetry	17
57	6.4.1	Electromagnetic Calorimeters	17
58	6.4.2	Hadronic Calorimeters	17
59	6.4.3	Forward Calorimeters	17
60	6.5	Muon Spectrometer	17
61	6.6	Trigger	17
62	6.6.1	Trigger Scheme	17
63	6.6.2	Missing Transverse Energy Triggers	17
64	7	EVENT RECONSTRUCTION	19
65	7.1	Tracks and Vertices	19

66	7.1.1	Track Reconstruction	19
67	7.1.2	Vertex Reconstruction	19
68	7.2	Jets	19
69	7.2.1	Topological Clustering	19
70	7.2.2	Jet Energy Scale	19
71	7.2.3	Jet Energy Scale Uncertainties	19
72	7.2.4	Jet Energy Resolution	19
73	7.3	Electrons	19
74	7.3.1	Electron Identification	19
75	7.4	Muons	19
76	7.4.1	Muon Identification	19
77	7.5	Missing Transverse Energy	19
78	IV	CALORIMETER RESPONSE	21
79	8	RESPONSE MEASUREMENT WITH SINGLE HADRONS	23
80	8.1	Dataset and Simulation	24
81	8.1.1	Data Samples	24
82	8.1.2	Simulated Samples	24
83	8.1.3	Event Selection	24
84	8.2	Inclusive Hadron Response	25
85	8.2.1	E/p Distribution	26
86	8.2.2	Zero Fraction	26
87	8.2.3	Neutral Background Subtraction	28
88	8.2.4	Corrected Response	28
89	8.3	Identified Particle Response	34
90	8.3.1	Decay Reconstruction	34
91	8.3.2	Identified Response	35
92	8.3.3	Additional Species in Simulation	37
93	8.4	Summary	38
94	9	JET ENERGY RESPONSE AND UNCERTAINTY	41
95	9.1	Motivation	41
96	9.2	Uncertainty Estimate	41
97	9.3	Summary	44
98	V	SEARCH FOR LONG-LIVED PARTICLES	47
99	10	LONG-LIVED PARTICLES IN ATLAS	49
100	10.1	Overview and Characteristics	49
101	10.2	Simulation	49
102	11	EVENT SELECTION	51
103	11.1	Trigger	51
104	11.2	Kinematics and Isolation	51
105	11.3	Standard Model Rejection	51
106	11.4	Ionization	51
107	11.4.1	dE/dx Calibration	51
108	11.4.2	Mass Estimation	51
109	12	BACKGROUND ESTIMATION	53

110	12.1	Background Sources	53
111	12.2	Prediction Method	53
112	12.3	Validation and Uncertainty	53
113	13	SYSTEMATIC UNCERTAINTIES AND RESULTS	55
114	13.1	Systematic Uncertainties	55
115	13.2	Final Yields	55
116	14	INTERPRETATION	57
117	14.1	Cross Sectional Limits	57
118	14.2	Mass Limits	57
119	14.3	Context for Long-Lived Searches	57
120	VI	CONCLUSIONS	59
121	15	SUMMARY AND OUTLOOK	61
122	15.1	Summary	61
123	15.2	Outlook	61
124	VII	APPENDIX	63
125	A	INELASTIC CROSS SECTION	65
126	B	APPENDIX TEST	67
127	B.1	Appendix Section Test	67
128	B.1.1	Appendix Subection Test	67
129	B.2	A Table and Listing	67
130	B.3	Some Formulas	68
131		BIBLIOGRAPHY	71

132 LIST OF FIGURES

133	Figure 1	The particle content of the Standard Model (SM).	8
134	Figure 2	An illustration (a) of the E/p variable used throughout this paper. The red energy deposits come from the charged particle targeted for measurement, while the blue energy deposits are from nearby neutral particles and must be subtracted. The same diagram (b) for the neutral-background selection, described in Section 8.2.3.	25
135			
136			
137			
138			
139			
140	Figure 3	The E/p distribution and ratio of simulation to data for isolated tracks with (a) $ \eta < 0.6$ and $1.2 < p/\text{GeV} < 1.8$ and (b) $ \eta < 0.6$ and $2.2 < p/\text{GeV} < 2.8$	26
141			
142			
143	Figure 4	The fraction of tracks as a function (a, b) of momentum, (c, d) of interaction lengths with $E \leq 0$ for tracks with positive (on the left) and negative (on the right) charge.	27
144			
145			
146			
147	Figure 5	$\langle E/p \rangle_{\text{BG}}$ as a function of the track momentum for tracks with (a) $ \eta < 0.6$, (b) $0.6 < \eta < 1.1$, and as a function of the track pseudorapidity for tracks with (c) $1.2 < p/\text{GeV} < 1.8$, (d) $1.8 < p/\text{GeV} < 2.2$	29
148			
149			
150			
151	Figure 6	$\langle E/p \rangle_{\text{COR}}$ as a function of track momentum, for tracks with (a) $ \eta < 0.6$, (b) $0.6 < \eta < 1.1$, (c) $1.8 < \eta < 1.9$, and (d) $1.9 < \eta < 2.3$	30
152			
153			
154	Figure 7	$\langle E/p \rangle_{\text{COR}}$ calculated using LCW-calibrated topological clusters as a function of track momentum for tracks with (a) zero or more associated topological clusters or (b) one or more associated topological clusters.	31
155			
156			
157			
158	Figure 8	Comparison of the $\langle E/p \rangle_{\text{COR}}$ for tracks with (a) less than and (b) greater than 20 hits in the TRT.	32
159			
160	Figure 9	Comparison of the $\langle E/p \rangle_{\text{COR}}$ for (a) positive and (b) negative tracks as a function of track momentum for tracks with $ \eta < 0.6$	32
161			
162			
163	Figure 10	Comparison of the E/p distributions for (a) positive and (b) negative tracks with $0.8 < p/\text{GeV} < 1.2$ and $ \eta < 0.6$, in simulation with the FTFP_BERT and QGSP_BERT physics lists.	33
164			
165			
166			
167	Figure 11	Comparison of the response of the hadronic calorimeter as a function of track momentum (a) at the EM-scale and (b) after the LCW calibration.	33
168			
169			
170	Figure 12	Comparison of the response of the EM calorimeter as a function of track momentum (a) at the EM-scale and (b) with the LCW calibration.	34
171			
172			

173	Figure 13	The reconstructed mass peaks of (a) K_S^0 , (b) Λ , and (c) $\bar{\Lambda}$ candidates.	35
174			
175	Figure 14	The E/p distribution for isolated (a) π^+ , (b) π^- , (c) proton, and (d) anti-proton tracks.	36
176			
177	Figure 15	The fraction of tracks with $E \leq 0$ for identified (a) π^+ and π^- , and (b) proton and anti-proton tracks	36
178			
179	Figure 16	The difference in $\langle E/p \rangle$ between (a) π^+ and π^- (b) p and π^+ , and (c) \bar{p} and π^-	37
180			
181	Figure 17	$\langle E/p \rangle_{\text{COR}}$ as a function of track momentum for (a) π^+ tracks and (b) π^- tracks.	38
182			
183	Figure 18	The ratio of the calorimeter response to single parti- cles of various species to the calorimeter response to π^+ with the physics list FTFP_BERT.	38
184			
185	Figure 19	The spectra of true particles inside anti- k_t , $R = 0.4$ jets with (a) $90 < p_T/\text{GeV} < 100$, (b) $400 < p_T/\text{GeV} <$ 500 , and (c) $1800 < p_T/\text{GeV} < 2300$	42
186			
187	Figure 20	The jet energy scale (JES) uncertainty contributions, as well as the total JES uncertainty, as a function of jet p_T for (a) $ \eta < 0.6$ and (b) $0.6 < \eta < 1.1$	44
188			
189	Figure 21	The JES correlations as a function of jet p_T and $ \eta $ for jets in the central region of the detector.	45
190			
191			
192			
193			

194 LIST OF TABLES

₂₀₀ LISTINGS

₂₀₁ Listing 1	A floating example (<code>listings</code> manual)	68
--------------------------	--	----

202 ACRONYMS

203 SM Standard Model

204 LCW local cluster weighted

205 MIP minimally ionizing particle

206 EPJC European Physical Journal C

207 JES jet energy scale

208

PART I

209

INTRODUCTION

210

You can put some informational part preamble text here.

1

211

212 INTRODUCTION

213

PART II

214

THEORETICAL CONTEXT

215

You can put some informational part preamble text here.

2

216

217 STANDARD MODEL

218 The SM of particle physics seeks to explain the symmetries and interactions of
219 all currently discovered fundamental particles. It has been tested by several genera-
220 tions of experiments and has been remarkably successful, no significant de-
221 viations have been found. The SM provides predictions in particle physics for
222 interactions up to the Planck scale (10^{15} - 10^{19} GeV).

223 The theory itself is a quantum field theory grown from an underlying $SU(3) \times$
224 $SU(2) \times U(1)$ that requires the particle content and quantum numbers consist-
225 ent with experimental observations (see Section 2.1). Each postulated symme-
226 try is accompanied by an interaction between particles through gauge invari-
227 ance. These interactions are referred to as the Strong, Weak, and Electromag-
228 netic forces, which are discussed in Section 2.2.

229 Although this model has been very predictive, the theory is incomplete; for
230 example, it is not able to describe gravity or astronomically observed dark matter.
231 These limitations are discussed in more detail in Section 2.3.

232 21 PARTICLES

233 The most familiar matter in the universe is made up of protons, neutrons, and
234 electrons. Protons and neutrons are composite particles, however, and are made
235 up in turn by particles called quarks. Quarks carry both electric charge and color
236 charge, and are bound in color-neutral combinations called baryons. The elec-
237 tron is an example of a lepton, and carries only electric charge. Another type
238 of particle, the neutrino, does not form atomic structures in the same way that
239 quarks and leptons do because it carries no color or electric charge. Collectively,
240 these types of particles are known as fermions, the group of particles with half-
241 integer spin.

242 There are three generations of fermions, although familiar matter is formed
243 predominantly by the first generation. The generations are identical except for
244 their masses, which increase in each generation by convention. In addition, each
245 of these particles is accompanied by an antiparticle, with opposite-sign quantum
246 numbers but the same mass.

247 The fermions comprise what is typically considered matter, but there are
248 additional particles that are mediators of interactions between those fermions.
249 These mediators are known as the gauge bosons, gauge in that their existence
250 is required by gauge invariance (discussed further in Section 2.2) and bosons in
251 that they have integer spin. The boson which mediates the electromagnetic force
252 is the photon, the first boson to be discovered; it has no electric charge, no mass,
253 and a spin of 1. There are three spin-1 mediators of the weak force, the two W
254 bosons and the Z boson. The W bosons have electric charge of ± 1 and a mass of
255 80.385 ± 0.015 GeV, while the Z boson is neutral and has a mass of $91.1876 \pm$

256 0.0021 GeV. The strong force is mediated by eight particles called gluons, which
 257 are massless and electrically neutral but do carry color charge.

258 The final particle present in the SM is the Higgs boson, which was recently
 259 observed for the first time by experiments at CERN in 2012. It is electrically
 260 neutral, has a mass of 125.7 ± 0.4 GeV, and is the only spin-0 particle yet to be
 261 observed. The Higgs boson is the gauge boson associated with the mechanism
 262 that gives a mass to the W and Z bosons.

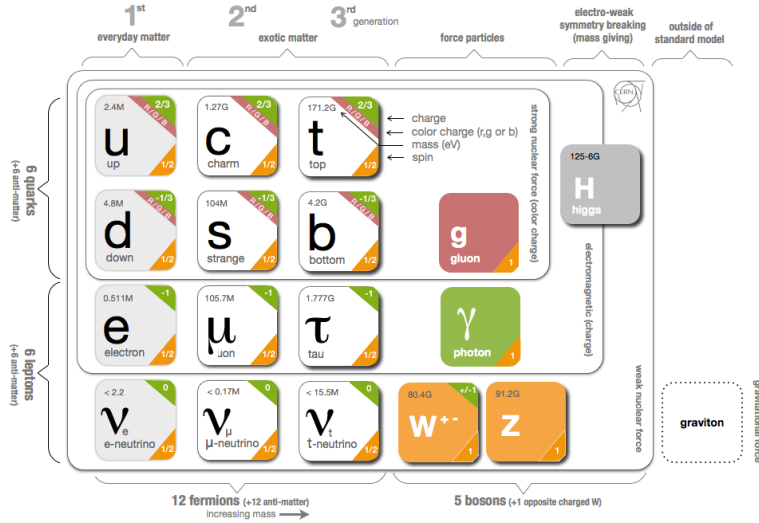


Figure 1: The particle content of the SM.

263 Together these particles form the entire content of the SM, and are summa-
 264 rized in Figure 1. These are the particles that constitute the observable universe
 265 and all the so-far-observed interactions within it.

266 2.2 INTERACTIONS

267 The interactions predicted and described by the SM are fundamentally tied to the
 268 particles within it, both in that they describe the way those particles can influence
 269 each other and also in that the existence of the interactions requires the existence
 270 of some particles (the gauge bosons).

271 2.3 LIMITATIONS

3

²⁷²

²⁷³ SUPERSYMMETRY

²⁷⁴ 3.1 MOTIVATION

²⁷⁵ 3.2 STRUCTURE

²⁷⁶ 3.3 PHENOMENOLOGY

4

277

278 LONG-LIVED PARTICLES

279 4.1 MECHANISMS

280 4.1.1 EXAMPLES IN SUPERSYMMETRY

281 4.2 PHENOMENOLOGY

282 4.2.1 DISIMILARITIES TO PROMPT DECAYS

283 4.2.2 CHARACTERISTIC SIGNATURES

284

PART III

285

EXPERIMENTAL STRUCTURE AND RECONSTRUCTION

286

You can put some informational part preamble text here.

5

287

288 THE LARGE HADRON COLLIDER

289 5.1 INJECTION CHAIN

290 5.2 DESIGN AND PARAMETERS

291 5.3 LUMINOSITY

6

292

293 THE ATLAS DETECTOR

294 6.1 COORDINATE SYSTEM

295 6.2 MAGNETIC FIELD

296 6.3 INNER DETECTOR

297 6.3.1 PIXEL DETECTOR

298 6.3.2 SEMICONDUCTOR TRACKER

299 6.3.3 TRANSITION RADIATION TRACKER

300 6.4 CALORIMETRY

301 6.4.1 ELECTROMAGNETIC CALORIMETERS

302 6.4.2 HADRONIC CALORIMETERS

303 6.4.3 FORWARD CALORIMETERS

304 6.5 MUON SPECTROMETER

305 6.6 TRIGGER

306 6.6.1 TRIGGER SCHEME

307 6.6.2 MISSING TRANSVERSE ENERGY TRIGGERS

7

308

309 EVENT RECONSTRUCTION

310 The ATLAS experiment combines measurements in the subdetectors to form a
311 cohesive picture of each physics event.

312 7.1 TRACKS AND VERTICES

313 7.1.1 TRACK RECONSTRUCTION

314 7.1.1.1 NEURAL NETWORK

315 7.1.1.2 PIXEL DE/DX

316 7.1.2 VERTEX RECONSTRUCTION

317 7.2 JETS

318 7.2.1 TOPOLOGICAL CLUSTERING

319 7.2.2 JET ENERGY SCALE

320 7.2.3 JET ENERGY SCALE UNCERTAINTIES

321 7.2.4 JET ENERGY RESOLUTION

322 7.3 ELECTRONS

323 7.3.1 ELECTRON IDENTIFICATION

324 7.4 MUONS

325 7.4.1 MUON IDENTIFICATION

326 7.5 MISSING TRANSVERSE ENERGY

327

PART IV

328

CALORIMETER RESPONSE

329

You can put some informational part preamble text here.

331 RESPONSE MEASUREMENT WITH SINGLE HADRONS

332 As discussed in Section 7.2, colored particles produced in collisions hadronize
333 into jets of multiple hadrons. One approach to understanding jet physics in the
334 ATLAS calorimetry is to evaluate the calorimeter response to those individual
335 hadrons; measurements of individual hadrons can be used to build up an under-
336 standing of the jets that they form. The redundancy of the momentum provided
337 by the tracking system and the energy provided by the calorimeter provides an
338 opportunity to study calorimeter response using real collisions, as described fur-
339 ther in Section 8.2.

340 Calorimeter response includes a number of physical effects that can be ex-
341 tracted to provide insight into many aspects of jet modeling. First, many charged
342 hadrons interact with the material of the detector prior to reaching the calorime-
343 ters and thus do not deposit any energy. Comparing this effect in data and sim-
344 ulation is a powerful tool in validating the interactions of particles with the ma-
345 terial of the detector and the model of the detector geometry in simulation, see
346 Section 8.2.2. The particles which do reach the calorimeter deposit their energy
347 into individual cells, which are then clustered to measure full energy deposits.
348 Comparing the response in data to simulated hadrons provides a direct evalua-
349 tion of noise in the calorimeters, the showering of hadronic particles, and the
350 energy deposited by particles in matter (Section 8.2.4). These measurements are
351 extended to explore several additional effects, such as the dependence on charge,
352 in Section 8.2.4.1.

353 The above studies all use an inclusive selection of charged particles, which are
354 comprised predominantly of pions, kaons, and (anti)protons. It is also possible
355 to measure the particle types separately to evaluate the simulated interactions of
356 each particle, particularly at low energies where differences between species are
357 very relevant. Pions and (anti)protons can be identified through decays of long-
358 lived particles, in particular Λ , $\bar{\Lambda}$, and K_S^0 , and then used to measure response as
359 described above. This is discussed in detail in Section 8.3.

360 Together, these measurements in data provide a thorough understanding of
361 the way hadrons interact with the ATLAS detector and can be used to build up a
362 description of jets, as seen in Chapter 9. The results in this chapter use data col-
363 lected at 7 and 8 TeV collected in 2010 and 2012, respectively. Both are included
364 as the calorimeter was repaired and recalibrated between those two data-taking
365 periods. Both sets of data are compared to an updated simulation that includes
366 new physics models provided by Geant4 [12] and improvements in the detec-
367 tor description [2, 6]. These results are published in European Physical Journal
368 C (EPJC) [8] and can be compared to a similar measurement performed in 2009
369 and 2010 [5], which used the previous version of the simulation framework [1].

370 8.1 DATASET AND SIMULATION

371 8.1.1 DATA SAMPLES

372 The two datasets used in this chapter are taken from dedicated low-pileup runs
 373 where the fraction of events with multiple interactions was negligible, to facilitate
 374 measurement of isolated hadrons. The 2012 dataset at $\sqrt{s} = 8$ TeV contains
 375 8 million events and corresponds to an integrated luminosity of 0.1 nb^{-1} . The
 376 2010 dataset at $\sqrt{s} = 7$ TeV contains 3 million events and corresponds to an
 377 integrated luminosity of 3.2 nb^{-1} . The latter dataset was also used in the 2010
 378 results [5], but it has since been reanalyzed with an updated detector description
 379 for the material and alignment.

380 8.1.2 SIMULATED SAMPLES

381 The two datasets above are compared to simulated single-, double-, and non-
 382 diffractive events generated with Pythia8 [32] using the A2 configuration of
 383 hadronization [3] and the MSTW 2008 parton-distribution function set [28, 31].
 384 The conditions and energies for each run are matched in the two simulations.

385 To evaluate the interaction of hadrons with detector material, the simulation
 386 uses two different collections of hadronic physics models, called physics lists, in
 387 Geant4 9.4 [30]. The first, QGSP_BERT, combines the Bertini intra-nuclear
 388 cascade [17, 24, 26] below 9.9 GeV, a parametrized proton inelastic model from
 389 9.5 to 25 GeV [21], and a quark-gluon string model above 12 GeV [13, 14, 18, 19,
 390 22]. The second, FTFP_BERT, combines the Bertini intra-nuclear cascade [17, 24,
 391 26] below 5 GeV and the Fritiof model [15, 16, 23, 29] above 4 GeV. In either list,
 392 Geant4 enforces a smooth transition between models where multiple models
 393 overlap.

394 8.1.3 EVENT SELECTION

395 The event selection for this study is minimal, as the only requirement is selecting
 396 good-quality events with an isolated track. Such events are triggered by requiring
 397 at least two hits in the minimum-bias trigger scintillators. After trigger, each
 398 event is required to have exactly one reconstructed vertex, and that vertex is re-
 399 quired to have four or more associated tracks.

400 The particles which enter into the response measurements are first identified
 401 as tracks in the inner detector. The tracks are required to have at least 500 MeV
 402 of transverse momentum. To ensure a reliable momentum measurement, these
 403 tracks are required to have at least one hit in the pixel detector, six hits in the SCT,
 404 and small longitudinal and transverse impact parameters with respect to the pri-
 405 mary vertex [5]. For the majority of the measurements in this chapter, the track is
 406 additionally required to have 20 hits in the TRT, which significantly reduces the
 407 contribution from tracks which undergo nuclear interactions. This requirement
 408 and its effect is discussed in more detail in Section 8.2.4.1. In addition, tracks are
 409 rejected if there is another track which extrapolates to the calorimeter within a

cone of $\Delta R = \sqrt{(\Delta\phi)^2 + (\Delta\eta)^2} < 0.4$. This requirement guarantees that the contamination of energy from nearby charged particles is negligible [5].

8.2 INCLUSIVE HADRON RESPONSE

The calorimeter response is more precisely defined as the ratio of the measured calorimeter energy to the true energy carried by the particle, although this true energy is unknown. For charged particles, however, the inner detector provides a very precise measurement of momentum (with uncertainty less than 1%) that can be used as a proxy for true energy. The ratio of the energy deposited by the charged particle in the calorimeter, E , to its momentum measured in the inner detector p , forms the calorimeter response measure called E/p . Though the distribution of E/p contains a number of physical features, this study focuses on the trends in two aggregated quantities: $\langle E/p \rangle$, the average of E/p within a given subset of particles, and the zero fraction, the fraction of particles with no associated energy in the calorimeter.

The calorimeter energy assigned to a track particle is defined using clusters. The clusters are formed using a 4–2–0 algorithm [9] that begins with seeds requiring at least 4 times the average calorimeter noise. The neighboring cells with at least twice that noise threshold are then added to the cluster, and all bounding cells are then added with no requirement. This algorithm minimizes noise contributions through its seeding process, and including the additional layers improves the energy resolution [33]. The clusters are associated to a given track if they fall within a cone of $\Delta R = 0.2$ of the extrapolated position of the track, which includes about 90% of the energy on average [5]. This construction is illustrated in Figure 2.

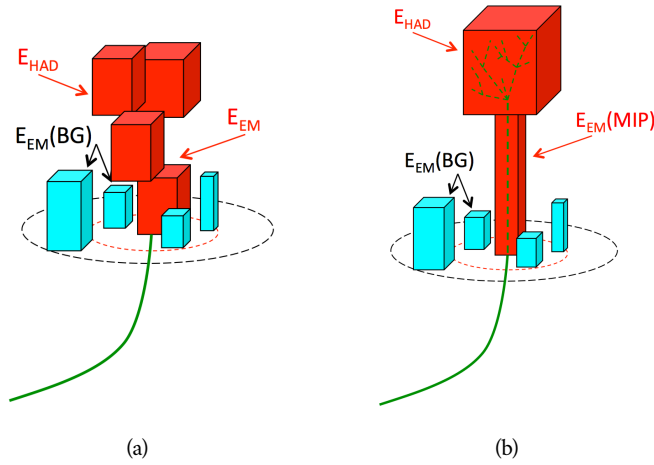


Figure 2: An illustration (a) of the E/p variable used throughout this paper. The red energy deposits come from the charged particle targeted for measurement, while the blue energy deposits are from nearby neutral particles and must be subtracted. The same diagram (b) for the neutral-background selection, described in Section 8.2.3.

434 8.2.1 E/P DISTRIBUTION

435 The E/p distributions measured in both data and simulation are shown in Figure 3 for two example bins of track momentum and for tracks in the central
 436 region of the detector. These distributions show several important features of
 437 the E/p observable. The large content in the bin at $E = 0$ comes from tracks that
 438 have no associated cluster, which occurs due to interactions with detector mate-
 439 rial prior to reaching the calorimeter or the energy deposit being insufficiently
 440 large to generate a seed, and are discussed in Section 8.2.2. The small negative
 441 tail comes from similar tracks that do not deposit any energy in the calorime-
 442 ter but are randomly associated to a noise cluster. The long positive tail above
 443 1.0 comes from the contribution of neutral particles. Nearby neutral particles
 444 deposit (sometimes large) additional energy in the calorimeter but do not pro-
 445 duce tracks in the inner detector, so they cannot be rejected by the track isol-
 446 ation requirement. Additionally the peak and mean of the distribution falls below
 447 1.0 because of the loss of energy not found within the cone as well as the non-
 448 compensation of the calorimeter.
 449

450 The data and simulation share the same features, but the high and low tails
 451 are significantly different. The simulated events tend to overestimate the contri-
 452 bution of neutral particles to the long tail, an effect which can be isolated and
 453 removed as discussed in Section 8.2.3. Additionally, the simulated clusters have
 454 less noise on average, although this is a small effect on the overall response.

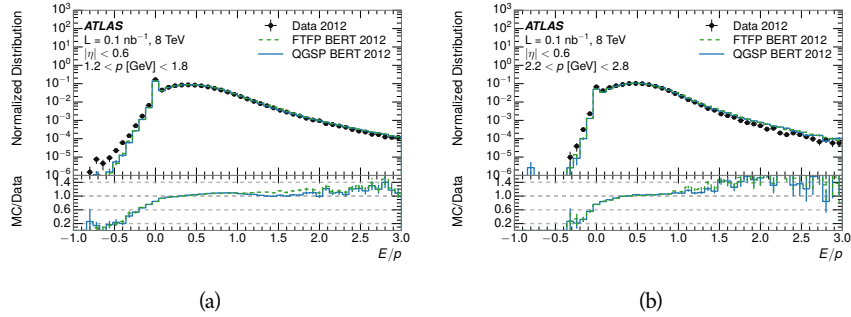


Figure 3: The E/p distribution and ratio of simulation to data for isolated tracks with
 (a) $|\eta| < 0.6$ and $1.2 < p/\text{GeV} < 1.8$ and (b) $|\eta| < 0.6$ and $2.2 < p/\text{GeV} < 2.8$.

455 8.2.2 ZERO FRACTION

456 The fraction of particles with no associated clusters, or similarly those with $E \leq$
 457 0, reflects the modeling of both the detector geometry and hadronic interactions.
 458 The zero fraction is expected to rise as the amount of material a particle traverses
 459 increases, while it is expected to decrease as the particle energy increases. This
 460 dependence can be seen in Figure 4, where the zero fraction in data and simula-
 461 tion is shown as a function of momentum and the amount of material measured
 462 in interaction lengths. The trends are similar between the 2010 and 2012 mea-
 463 surements. The zero fraction decreases with energy as expected. The amount of

material in the detector increases with η , which provides a distribution of interaction lengths. As the data and simulation have significant disagreement in the zero fraction over a number of interaction lengths, the difference must be primarily from the modeling of hadronic interactions with detector material and not just the detector geometry.

There is also a noticeable difference between positive and negative tracks at low momentum, which reflects the difference in response between protons and antiprotons. Antiprotons have significant model differences in the two physics lists, QGSP_BERT and FTFP_BERT, and this is evident in the lowest momentum bin of the data to simulation ratio. This difference is explored further in Section 8.3.

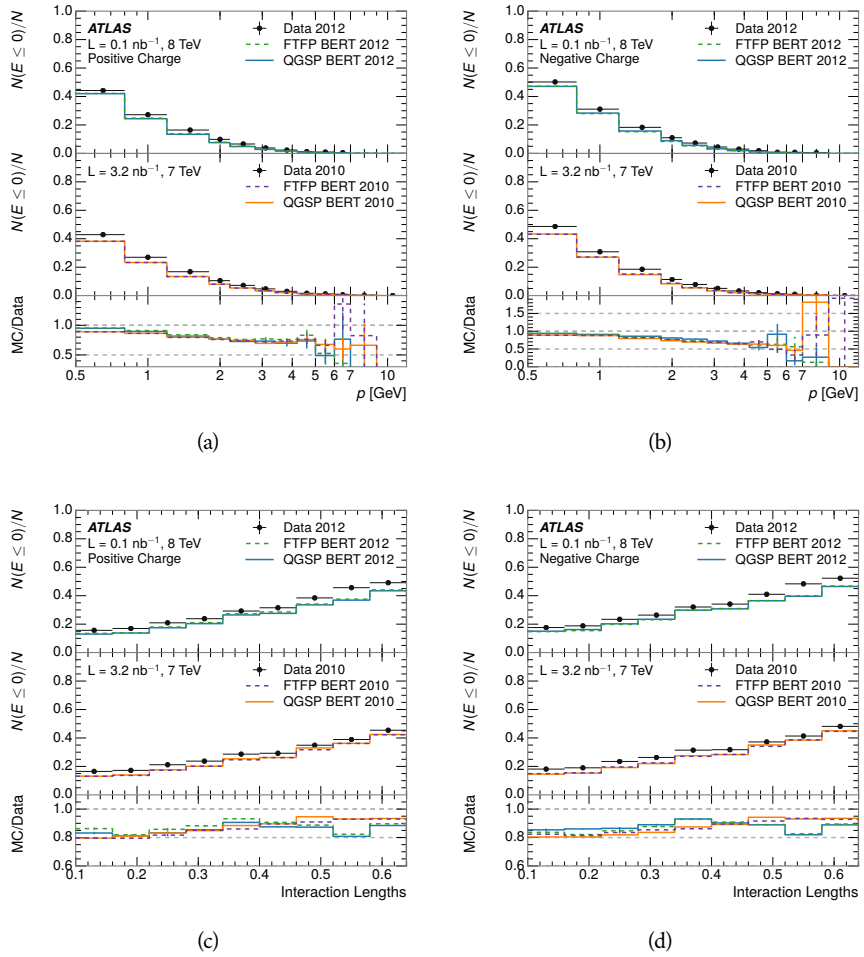


Figure 4: The fraction of tracks as a function (a, b) of momentum, (c, d) of interaction lengths with $E \leq 0$ for tracks with positive (on the left) and negative (on the right) charge.

475 8.2.3 NEUTRAL BACKGROUND SUBTRACTION

476 The isolation requirement on hadrons is only effective in remove energy contri-
 477 bution from nearby charged particles. Nearby neutral particles, predominantly
 478 photons from π^0 decays, also add their energy to the calorimeter clusters, but
 479 mostly in the electromagnetic calorimeter. It is possible to measure this contri-
 480 bution, on average, using late-showering hadrons that minimally ionize in the
 481 electromagnetic calorimeter. Such particles are selected by requiring that they
 482 deposit less than 1.1 GeV in the EM calorimeter within a cone of $\Delta R < 0.1$
 483 around the track. To ensure that these particles are well measured, they are addi-
 484 tionally required to deposit between 40% and 90% of their energy in the hadronic
 485 calorimeter within the same cone.

486 These particles provide a clean sample to measure the nearby neutral back-
 487 ground because they do not deposit energy in the area immediately surrounding
 488 them in the EM calorimeter, as shown in Figure 2. So, the energy deposits in the
 489 region $0.1 < \Delta R < 0.2$ can be attributed to neutral particles alone. To estimate
 490 the contribution to the whole cone considered for the response measurement,
 491 that energy is scaled by a geometric factor of 4/3. This quantity, $\langle E/p \rangle_{\text{BG}}$, mea-
 492 sured in aggregate over a number of particles, gives the contribution to $\langle E/p \rangle$
 493 from neutral particles in the EM calorimeter. Similar techniques were used in
 494 the individual layers of the hadronic calorimeters to show that the background
 495 from neutrals is negligible in those layers [5].

496 The distribution of this background estimate is shown in Figure 5. Although
 497 the simulation captures the overall trend, it significantly overestimates the neu-
 498 tral contribution for tracks with momentum between 2 and 8 GeV. This effect
 499 was also seen in the tails of the E/p distributions in Figure 3. This difference is
 500 likely due to the modeling of coherent neutral particle radiation in Pythia8, as
 501 the discrepancy does not depend on η and thus is unlikely to be a mismodeling
 502 of the detector. This difference can be subtracted to form a corrected average
 503 E/p , as in Section 8.2.4.

504 8.2.4 CORRECTED RESPONSE

505 Figure 6 shows $\langle E/p \rangle_{\text{COR}}$ as a function of momentum for several bins of pseu-
 506 dorapidity. This corrected $\langle E/p \rangle_{\text{COR}} \equiv \langle E/p \rangle - \langle E/p \rangle_{\text{BG}}$ measures the average
 507 calorimeter response without the contamination of neutral particles. It is the
 508 most direct measurement of calorimeter response in that it is the energy mea-
 509 sured for fully isolated hadrons. The correction is performed separately in data
 510 and simulation, so that the mismodeling of the neutral background in simulation
 511 is removed from the comparison of response. The simulation overestimates the
 512 response at low momentum by about 5%, an effect that can be mostly attributed
 513 to the underestimation of the zero fraction mentioned previously.

514 The response measurement above used topological clustering at the EM scale,
 515 that is clusters were formed to measure energy but no corrections were applied
 516 to correct for expected effects like energy lost outside of the cluster or in unin-
 517 strumented material. It is also interesting to measure $\langle E/p \rangle_{\text{COR}}$ using local clus-

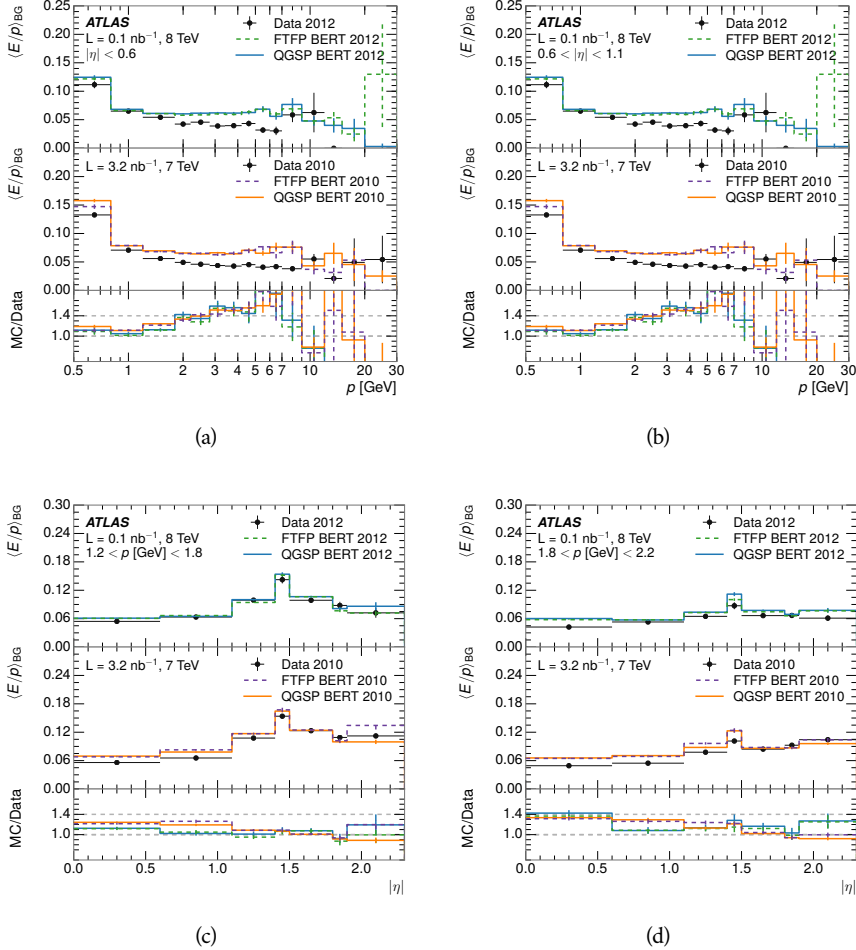


Figure 5: $\langle E/p \rangle_{BG}$ as a function of the track momentum for tracks with (a) $|\eta| < 0.6$, (b) $0.6 < |\eta| < 1.1$, and as a function of the track pseudorapidity for tracks with (c) $1.2 < p/\text{GeV} < 1.8$, (d) $1.8 < p/\text{GeV} < 2.2$.

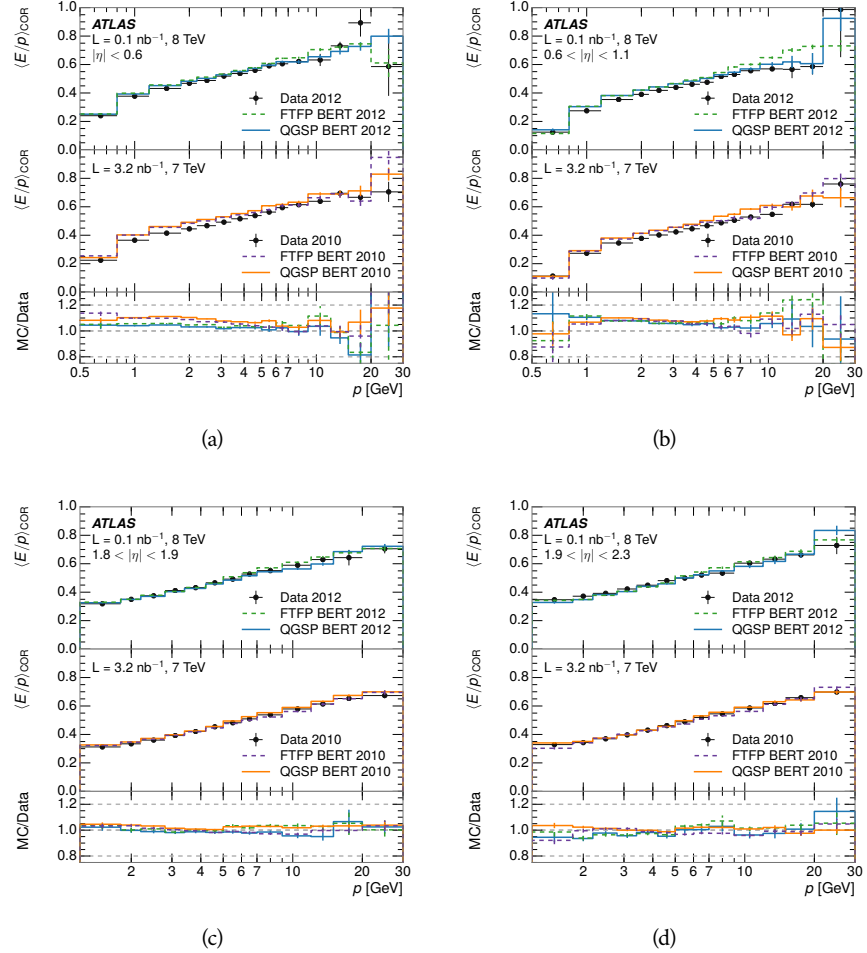


Figure 6: $\langle E/p \rangle_{\text{COR}}$ as a function of track momentum, for tracks with (a) $|\eta| < 0.6$, (b) $0.6 < |\eta| < 1.1$, (c) $1.8 < |\eta| < 1.9$, and (d) $1.9 < |\eta| < 2.3$.

518 ter weighted (LCW) energies, which accounts for those effects by calibrating the
 519 energy based on the properties of the cluster such as energy density and depth
 520 in the calorimeter. Figure 7 shows these distributions for tracks with zero or
 521 more clusters and separately for tracks with one or more clusters. The calibra-
 522 tion moves $\langle E/p \rangle_{\text{COR}}$ significantly closer to 1.0, which is the purpose of the cali-
 523 bration. The agreement between data and simulation improves noticeably when
 524 at least one cluster is required, as this removes the contribution from the mis-
 525 modeling of the zero fraction.

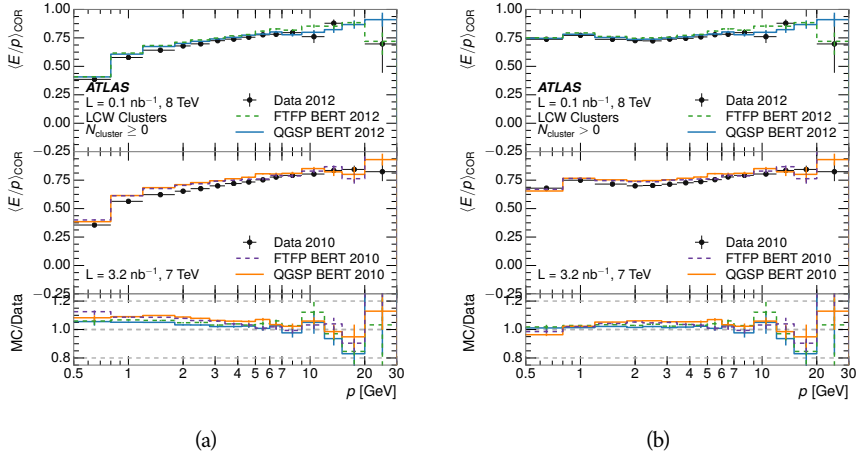


Figure 7: $\langle E/p \rangle_{\text{COR}}$ calculated using LCW-calibrated topological clusters as a function of track momentum for tracks with (a) zero or more associated topological clusters or (b) one or more associated topological clusters.

526 8.2.4.1 ADDITIONAL STUDIES

527 As has been seen in several previous measurements, the simulation does not
 528 correctly model the chance of a low momentum hadron to reach the calorime-
 529 ter. Because of the consistent discrepancy across pseudorapidity and interaction
 530 lengths, this seems to be best explained by incomplete understanding of hadronic
 531 interactions with the detector. For example, a hadron that scatters off of a nu-
 532 cleus in the inner detector can be deflected through a significant angle and not
 533 reach the expected location in the calorimeter. In addition, these interactions can
 534 produce secondary particles that are difficult to model.

535 The requirement on the number of hits in the TRT reduces these effects by
 536 preferentially selecting tracks that do not undergo nuclear interactions. It is in-
 537 teresting to check how well the simulation models tracks with low numbers of
 538 TRT hits, where the nuclear interactions are much more likely. Figure 8 com-
 539 pares the distributions with $N_{\text{TRT}} < 20$ to $N_{\text{TRT}} > 20$ for real and simulated
 540 particles. As expected, the tracks with fewer hits are poorly modeled in the sim-
 541 ulation as $\langle E/p \rangle_{\text{COR}}$ differs by as much as 25% at low momentum.

542 Another interesting aspect of the simulation is the description of antiprotons
 543 at low momentum, where QGSP_BERT and FTFP_BERT have significant differ-
 544 ences. This can be seen to have an effect in the inclusive response measurement

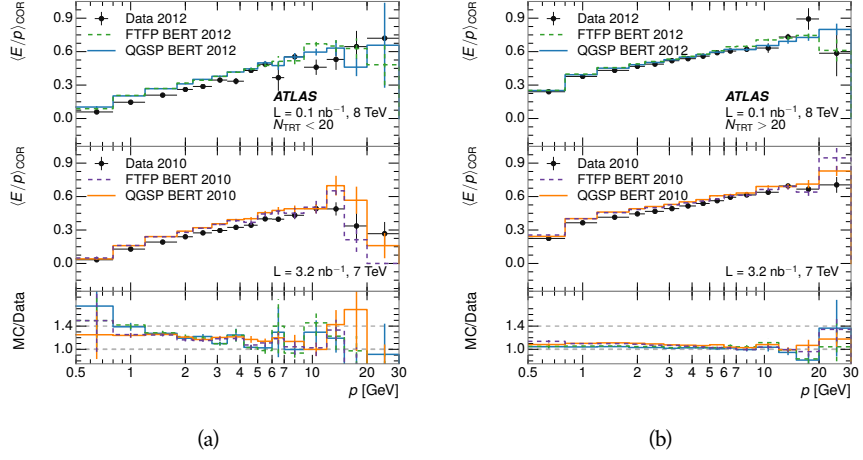


Figure 8: Comparison of the $\langle E/p \rangle_{\text{COR}}$ for tracks with (a) less than and (b) greater than 20 hits in the TRT.

when separated into positive and negative charge. The $\langle E/p \rangle_{\text{COR}}$ distributions for positive and negative particles are shown in Figure 9, where a small difference between QGSP_BERT and FTFP_BERT can be seen in the distribution for negative tracks. This is demonstrated more clearly in Figure 10, which shows the E/p distribution in the two simulations separated by charge. There is a clear difference around $E/p > 1.0$, which can be explained by the additional energy deposited by the annihilation of the antiproton in the calorimeter that is modeled well only in FTFP_BERT. This is also explored with data using identified antiprotons in Section 8.3.

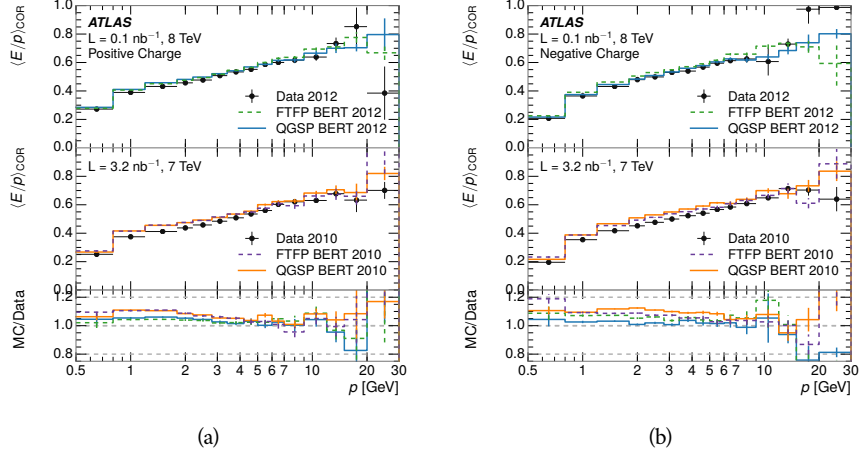


Figure 9: Comparison of the $\langle E/p \rangle_{\text{COR}}$ for (a) positive and (b) negative tracks as a function of track momentum for tracks with $|\eta| < 0.6$.

The $\langle E/p \rangle$ results in previous sections have considered the electromagnetic and hadronic calorimeters together as a single energy measurement, to emphasize the total energy deposited for a given particle. However, the deposits in each

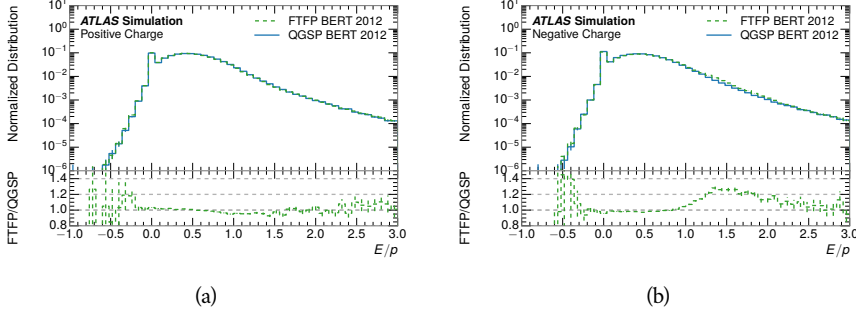


Figure 10: Comparison of the E/p distributions for (a) positive and (b) negative tracks with $0.8 < p/\text{GeV} < 1.2$ and $|\eta| < 0.6$, in simulation with the FTFP_BERT and QGSP_BERT physics lists.

557 calorimeter are available separately and $\langle E/p \rangle$ can be constructed for each layer.
 558 As the layers are composed of different materials and are modeled separately in
 559 the detector geometry, confirmation that the simulation matches the data well
 560 in each layer adds confidence in both the description of hadronic interactions
 561 with the two different materials and also the geometric description of each.

562 The technique discussed in Section 8.2.3 for selecting minimally ionizing par-
 563 ticle (**MIP**s) in the electromagnetic calorimeter is also useful in studying deposits
 564 in the hadronic calorimeter. Those **MIP**s deposit almost all of their energy ex-
 565 clusively in the hadronic calorimeter. Figure 11 shows $\langle E/p \rangle_{\text{Had}}^{\text{Raw}}$, where **RAW**
 566 indicates that no correction has been applied for neutral backgrounds and **Had**
 567 indicates that only clusters for the hadronic calorimeter are included. The **RAW**
 568 and **COR** versions of $\langle E/p \rangle$ in this case are the same, as the neutral background
 569 is negligible in that calorimeter layer. The distributions are shown both for the
 570 original EM scale calibration and after LCW calibration. The data and simulation
 571 agree very well in this comparison, except in the lowest momentum bin which
 572 has 5% discrepancy that has already been seen in similar measurements.

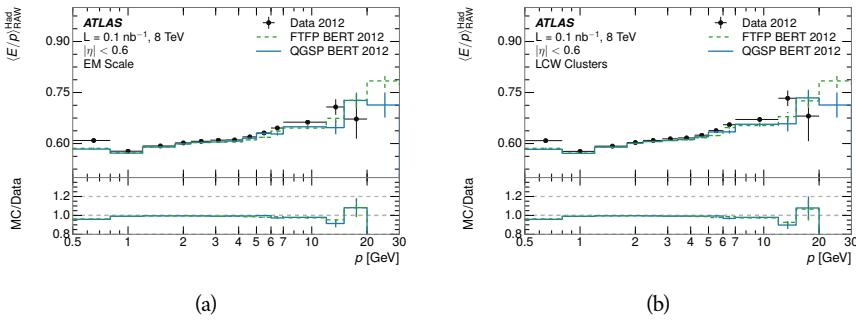


Figure 11: Comparison of the response of the hadronic calorimeter as a function of track momentum (a) at the EM-scale and (b) after the LCW calibration.

573 A similar comparison can be made in the electromagnetic calorimeter by se-
 574 lecting particles which have no associated energy in the hadronic calorimeter.
 575 These results are measured in terms of $\langle E/p \rangle_{\text{COR}}^{\text{EM}}$, where **EM** designates that

576 only clusters in the electromagnetic calorimeter are included and COR designates that the neutral background is subtracted as the neutral background is
 577 present in this case. Figure 12 shows the analogous comparisons to Figure 11 in
 578 the electromagnetic calorimeter. In this case the disagreement between data and
 579 simulation is more pronounced, with discrepancies as high as 5% over a larger
 580 range of momenta. This level of discrepancy indicates that the description of the
 581 electromagnetic calorimeter is actually the dominant source of discrepancy in
 582 the combined distributions in Section 8.2.4.

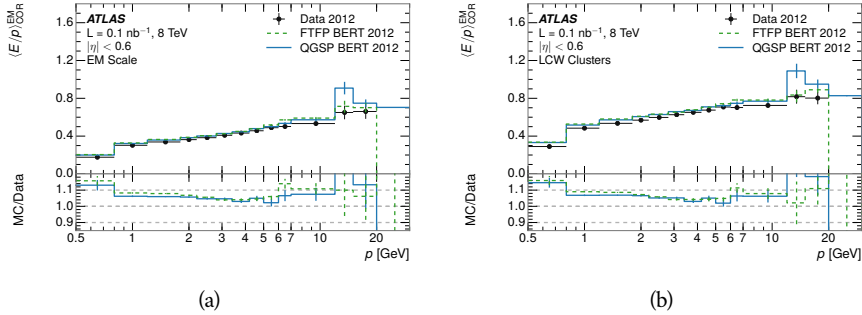


Figure 12: Comparison of the response of the EM calorimeter as a function of track momentum (a) at the EM-scale and (b) with the LCW calibration.

584 **NOTE: There are more studies that I skipped for brevity that could be**
 585 **included if interesting. E/p at different cluster threshold settings, E/p with**
 586 **pileup, E/p with cells. I also left out a lot of eta bins that appear in the paper**
 587 **so that this section didn't turn into 20 pages of plots.**

588 8.3 IDENTIFIED PARTICLE RESPONSE

589 The inclusive response measurement for hadrons can be augmented by measuring
 590 the response for specific particle species. The simulation models each parti-
 591 cle type separately, and understanding the properties of each is important in con-
 592 straining the uncertainty on jets. In order to select and measure specific hadrons,
 593 this section relies on the displaced decays of long-lived particles. Such decays can
 594 be identified by reconstructing secondary vertices with a requirement on mass.
 595 In particular, Λ , $\bar{\Lambda}$, and K_S^0 can be used to select a pure sample of protons, an-
 596 tiprotons, and pions, respectively.

597 8.3.1 DECAY RECONSTRUCTION

598 The measurement of response for identified particles uses the same selection
 599 as for inclusive particles (Section 8.1.3) with a few additions. Each event used
 600 is required to have at least one secondary vertex, and the tracks are required
 601 to match to that vertex rather than the primary vertex. Pions are selected from
 602 decays of $K_S^0 \rightarrow \pi^+ \pi^-$, which is the dominant decay for K_S^0 to charged particles.
 603 Protons are selected from decays of $\Lambda \rightarrow \pi^- p$ and antiprotons from $\bar{\Lambda} \rightarrow \pi^+ \bar{p}$,

which are similarly the dominant decays of Λ and $\bar{\Lambda}$ to charged particles. The species of parent hadron in these decays is determined by reconstructing the mass of the tracks associated to the secondary vertex. The sign of the higher momentum decay particle can distinguish between Λ and $\bar{\Lambda}$, which of course have the same mass, as the proton or antiproton is kinematically favored to have higher momentum. Examples of the reconstructed masses used to select these decays are shown in Figure 13.

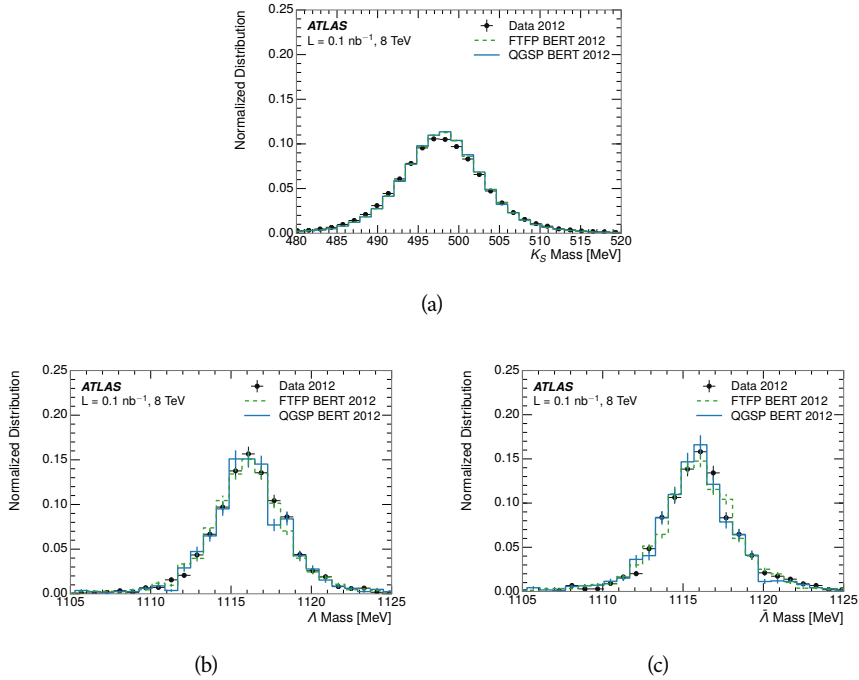


Figure 13: The reconstructed mass peaks of (a) K_S^0 , (b) Λ , and (c) $\bar{\Lambda}$ candidates.

The dominant backgrounds for the identified particle decays are nuclear interactions and combinatoric sources. These are suppressed by the kinematic requirements on the tracks as well as an additional veto which removes candidates that are consistent with both a Λ or $\bar{\Lambda}$ and a K_S^0 hypothesis, which is possible because of the different assumptions on particle mass in each case [5]. After these requirements, the backgrounds are found to be negligible compared to the statistical errors on these measurements.

8.3.2 IDENTIFIED RESPONSE

With these techniques the E/p distributions are extracted in data and simulation for each particle species and shown in Figure 14. These distributions are shown for a particular bin of E_a ($2.2 < E_a/\text{GeV} < 2.8$), rather than p . E_a is the energy available to be deposited in the calorimeter: for pions $E_a = \sqrt{p^2 + m^2}$, for protons $E_a = \sqrt{p^2 + m^2} - m$, and for antiprotons $E_a = \sqrt{p^2 + m^2} + m$. The features of the E/p distributions are similar to the inclusive case. There is a small negative tail from noise and a large fraction of tracks with zero energy from particles which do not reach the calorimeter. The long positive tail is noticeably more

627 pronounced for antiprotons because of the additional energy generated by the
 628 annihilation in addition to the neutral background.

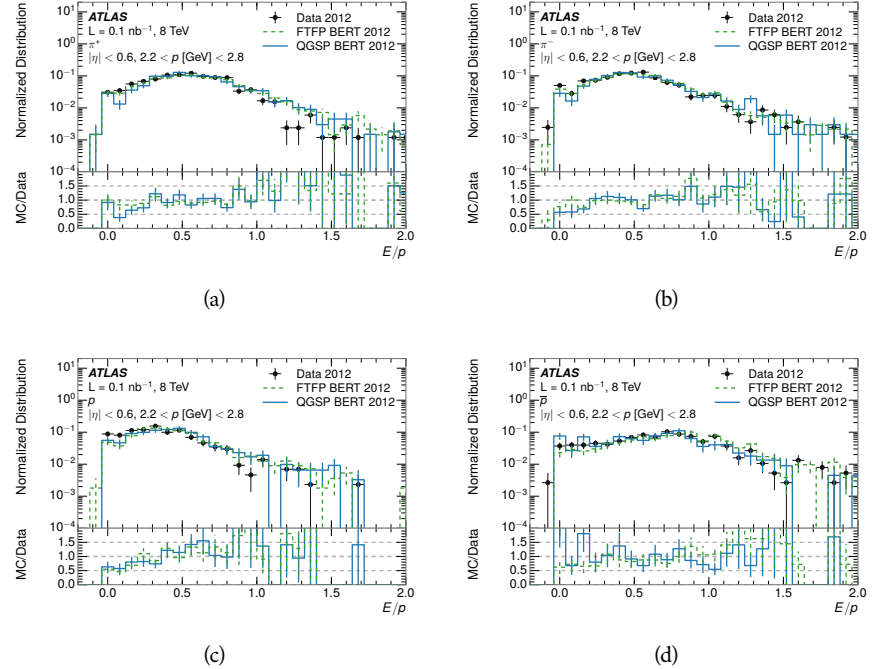


Figure 14: The E/p distribution for isolated (a) π^+ , (b) π^- , (c) proton, and (d) anti-proton tracks.

629 The zero fraction is further explored in Figure 15 for pions and protons in
 630 data and simulation. The simulation consistently underestimates the zero frac-
 631 tion independent of particle species, which implies that this discrepancy is not
 632 caused by the model of a particular species but rather a feature common to all.

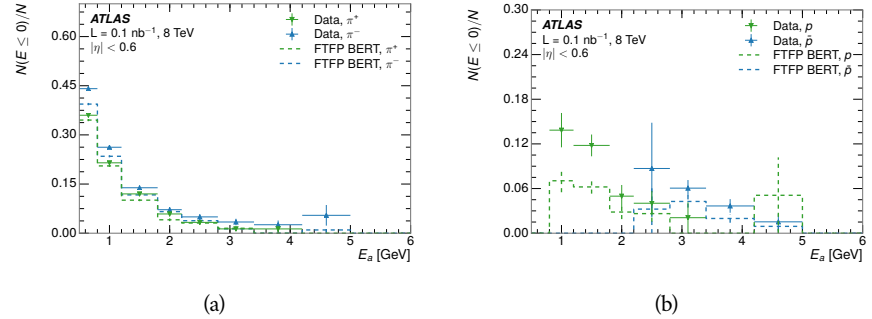


Figure 15: The fraction of tracks with $E \leq 0$ for identified (a) π^+ and π^- , and (b) proton and anti-proton tracks

633 It is also interesting to compare the response between the different particle
 634 species. One approach to do this is to measure the difference in $\langle E/p \rangle$ between
 635 two types, which has the advantage of removing the neutral background. These
 636 differences are shown in various combinations in Figure 16. The response for

637 π^+ is greater on average than the response to π^- because of a charge-exchange
 638 effect which causes the production of additional neutral pions in the showers of
 639 π^+ [20]. The response for π^+ is also greater on average than the response to p ,
 640 because a large fraction of the energy of π^+ hadrons is converted to an electro-
 641 magnetic shower [11, 25]. However, the \bar{p} response is significantly higher than
 642 the response to π^- because of the annihilation of the antiproton. FTFP_BERT
 643 does a better job of modeling this effect than QGSP_BERT because of their differ-
 644 ent descriptions of \bar{p} interactions with material.

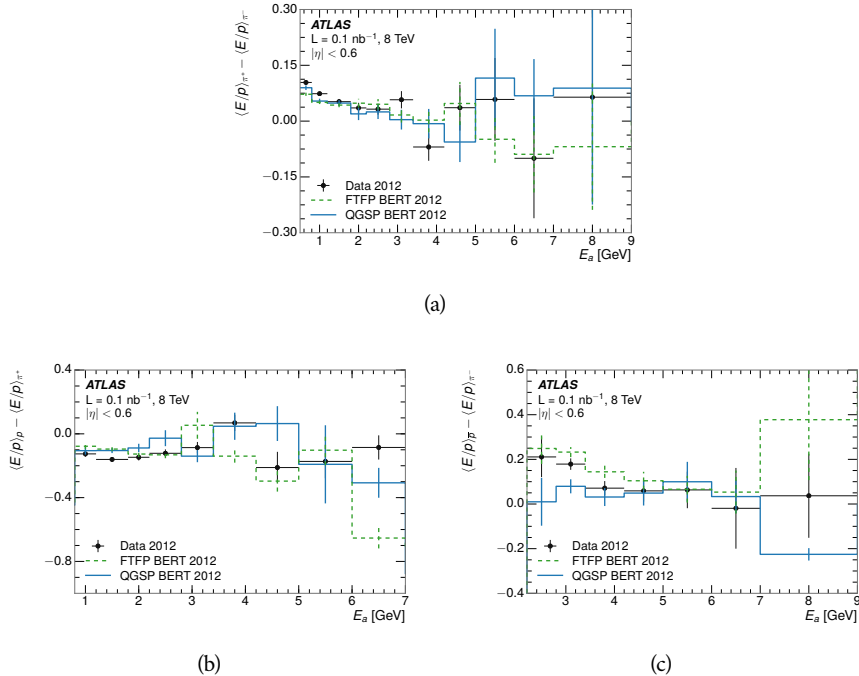


Figure 16: The difference in $\langle E/p \rangle$ between (a) π^+ and π^- (b) p and π^+ , and (c) \bar{p} and π^- .

645 It is also possible to remove the neutral background from these response dis-
 646 tributions using the same technique as in Section 8.2.3. The technique is largely
 647 independent of the particle species and so can be directly applied to $\langle E/p \rangle$ for
 648 pions. The $\langle E/p \rangle_{\text{COR}}$ distributions for pions are shown in Figure 17, which are
 649 very similar to the inclusive results. The inclusive hadrons are comprised mostly
 650 of pions, so this similarity is not surprising. It is also possible to see the small
 651 differences between π^+ and π^- response here, where $\langle E/p \rangle_{\text{COR}}$ is higher on av-
 652 erage for π^+ . The agreement between data and simulation is significantly worse
 653 for the π^- distributions than for the π^+ , with a discrepancy greater than 10%
 654 below 2-3 GeV.

655 8.3.3 ADDITIONAL SPECIES IN SIMULATION

656 The techniques above provide a method to measure the response separately for
 657 only pions and protons. However the hadrons which forms jets include a num-
 658 ber of additional species such as kaons and neutrons. The charged kaons are

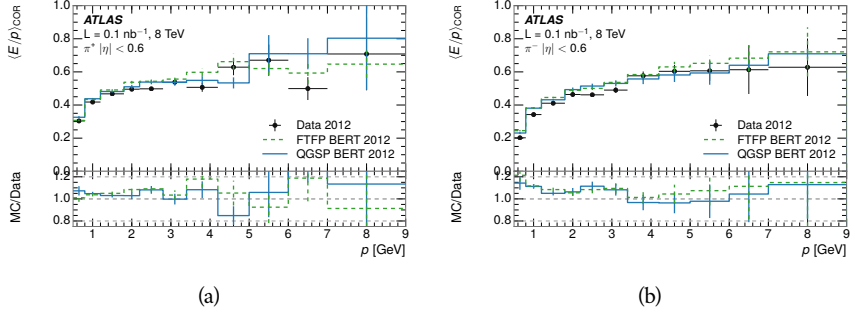


Figure 17: $\langle E/p \rangle_{\text{COR}}$ as a function of track momentum for (a) π^+ tracks and (b) π^- tracks.

659 an important component of the inclusive charged hadron distribution, which is
660 comprised of roughly 60-70% pions, 15-20% kaons, and 5-15% protons. These
661 are difficult to measure in data at the ATLAS detector, although a template sub-
662 tracton technique has been proposed which may be effective with larger sam-
663 ple sizes [8]. The simulation of these particles includes noticeable differences in
664 response at low energies, which are shown in Figure 18 for FTFP_BERT. The
665 significant differences in response between low energy protons and antiprotons
666 are accounted for above in the definitions of E_a .

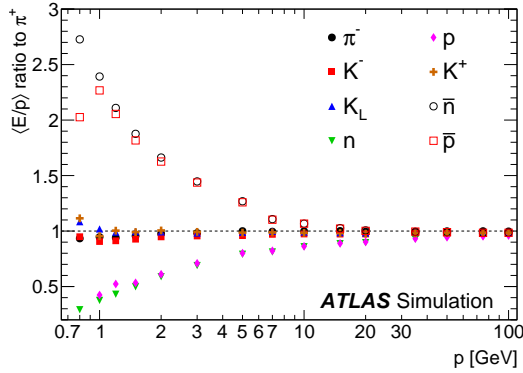


Figure 18: The ratio of the calorimeter response to single particles of various species to the calorimeter response to π^+ with the physics list FTFP_BERT.

667 8.4 SUMMARY

668 These various measurements of calorimeter response shown above for data and
669 simulation illuminate the accuracy of the simulation of hadronic interactions at
670 the ATLAS detector. The results were done using 2010 and 2012 data at 7 and 8
671 TeV, but reflect the most current understanding of the detector alignment and
672 geometry. A number of measurements focusing on a comparison between pro-
673 tons and antiprotons suggest that FTFP_BERT models those interaction more
674 accurately than QGSP_BERT. These measurements, among others, were the moti-

675 vation to switch the default **Geant4** simulation from **FTFP_BERT** to **QGSP_BERT**
676 for all ATLAS samples.

677 Even with these updates, there are a number of small, approximately 5%, dis-
678 crepancies in response between the data and simulation at low energies. At higher
679 energies the simulation of hadronic interactions is very consistent with data.
680 Chapter 9 discusses how to use these observed differences to constrain the jet
681 energy scale and its associated uncertainties.

682

683 JET ENERGY RESPONSE AND UNCERTAINTY

684 9.1 MOTIVATION

685 As jets form a major component of many physics analyses at ATLAS, it is crucial
 686 to carefully calibrate the measurement of jet energies and to derive an uncer-
 687 tainty on that measurement. These uncertainties have often been the dominant
 688 systematic uncertainty in high-energy analyses at the LHC. Dijet and multijet bal-
 689 ance techniques provide a method to constrain the [JES](#) and its uncertainty in data,
 690 and provide the default values used for ATLAS jet measurements at most ener-
 691 gies [7]. These techniques are limited by their reliance on measuring jets in data,
 692 so they are statistically limited in estimating the jet energy scale at the highest
 693 jet energies. This chapter presents another method for estimating the jet energy
 694 scale and its uncertainty which builds up a jet from its components and thus can
 695 be naturally extended to high jet momentum. Throughout this chapter the jets
 696 studied are simulated using [Pythia8](#) with the CT10 parton distribution set [27]
 697 and the AU2 tune [3], and corrections are taken from the studies including data
 698 and simulation in Chapter 8.

699 As described in Section 7.2, jets are formed from topological clusters of energy
 700 in the calorimeters using the anti- k_t algorithm. These clusters originate from a
 701 diverse spectrum of particles, in terms of both species and momentum, leading to
 702 significantly varied jet properties and response between jets of similar produced
 703 momentum. Figure 19 shows the simulated distribution of particles within jets
 704 at a few examples energies. The E/p measurements provide a thorough under-
 705 standing of the dominant particle content of jets, the charged hadrons.

706 9.2 UNCERTAINTY ESTIMATE

707 Simulated jets are not necessarily expected to correctly model the energy de-
 708 posits in the calorimeters, because of the various discrepancies discussed in Chap-
 709 ter 8. To evaluate a jet energy response, the simulated jet energies are compared
 710 to a corrected jet built up at the particle level. Each cluster in a jet is associated
 711 to the truth particle which deposited it, and the energy in that cluster is then
 712 corrected for a number of effects based on measurements in data. The primary
 713 corrections come from the single hadron response measurements in addition to
 714 response measured using the combined test beam which covers higher momen-
 715 tum particles [10]. These corrections include both a shift (Δ), in order to make the
 716 simulation match the average response in data, and an uncertainty (σ) associated
 717 with the ability to constrain the difference between data and simulation. Some of
 718 the dominant sources of uncertainty are itemized in Table ?? with typical values,
 719 and the full list considered is described in detail in the associated paper [8]. These

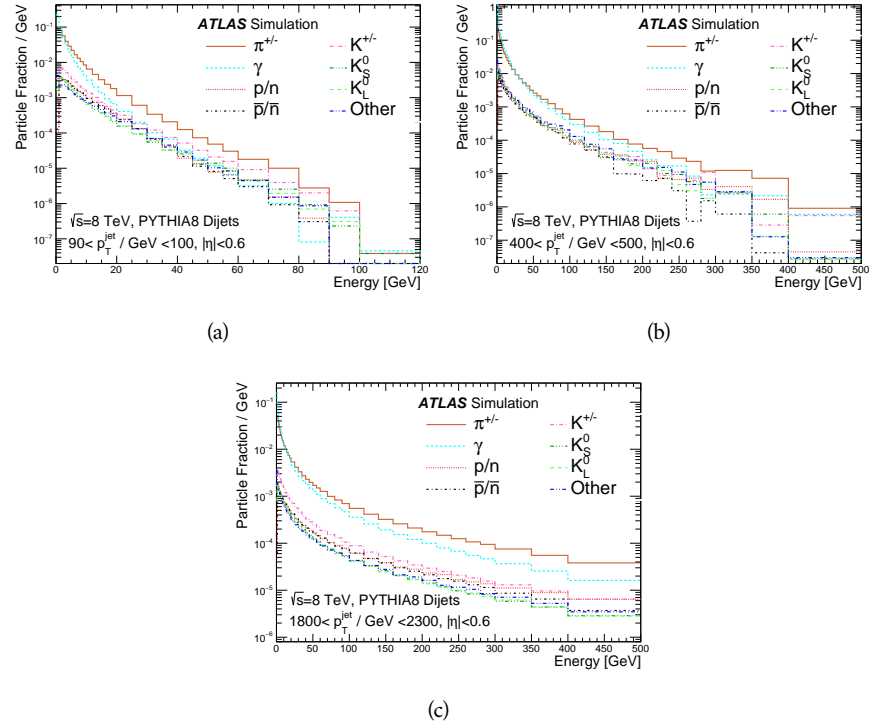


Figure 19: The spectra of true particles inside anti- k_t , $R = 0.4$ jets with (a) $90 < p_T/\text{GeV} < 100$, (b) $400 < p_T/\text{GeV} < 500$, and (c) $1800 < p_T/\text{GeV} < 2300$.

720 uncertainties cover differences between the data and simulation in the modeling
 721 of calorimeter response to a given particle. No uncertainties are added for the
 722 difference between particle composition of jets in data and simulation.

723 From these terms, the jet energy scale and uncertainty is built up from individual
 724 energy deposits in simulation. Each uncertainty term is treated independently,
 725 and are taken to be gaussian distributed. The resulting scale and uncertainty
 726 is shown in Figure 20, where the mean response is measured relative to the
 727 calibrated energy reported by simulation. The dominant uncertainties come
 728 from the statistical uncertainties on the E/p measurements at lower energies and
 729 the additional uncertainty for out of range measurements at higher energies. The
 730 total uncertainty from this method at intermediate jet energies is comparable to
 731 other simulation-based methods [4] and is about twice as large as in-situ meth-
 732 ods using data [7]. This method is the only one which provides an estimation
 733 above 1.8 TeV, however, and so is still a crucial technique in analyses that search
 734 for very energetic jets.

735 These techniques can also be used to measure the correlation between bins of
 736 average reconstructed jet momentum across a range of p_T and $|\eta|$, where cor-
 737 relations are expected because of a similarity in particle composition at similar
 738 energies. Figure 21 shows these correlations, where the uncertainties on jets in
 739 neighboring bins are typically between 30% and 60% correlated. The uncertainty
 740 on all jets becomes significantly correlated at high energies and larger pseudora-
 741 pidities, when the uncertainty becomes dominated by the single term reflecting
 742 out of range particles.

Abbrev.	Description	Δ (%)	σ (%)
In situ E/p	The comparison of $\langle E/p \rangle_{\text{COR}}$ as described in Chapter 8 with statistical uncertainties from 500 MeV to 20 GeV.	0-3	1-5
CTB	The main $\langle E/p \rangle$ comparison uncertainties, binned in p and $ \eta $, as derived from the combined test beam results, from 20 to 350 GeV [10].	0-3	1-5
E/p Zero Fraction	The difference in the zero-fraction between data and MC simulation from 500 MeV to 20 GeV.	5-25	1-5
E/p Threshold	The uncertainty in the EM calorimeter response from the potential mismodeling of threshold effects in topological clustering.	0	0-10
Neutral	The uncertainty in the calorimeter response to neutral hadrons based on studies of physics model variations.	0	5-10
K_L	An additional uncertainty in the response to neutral K_L in the calorimeter based on studies of physics model variations.	0	20
E/p Misalignment	The uncertainty in the p measurement from misalignment of the ID.	0	1
Hadrons, $p > 350$ GeV	A flat uncertainty for all particles above the energy range or outside the longitudinal range probed with the combined test beam.	0	10

Table 1: The dominant sources of corrections and systematic uncertainties in the [JES](#) estimation technique, including typical values for the correcting shift (Δ) and the associated uncertainty (σ).

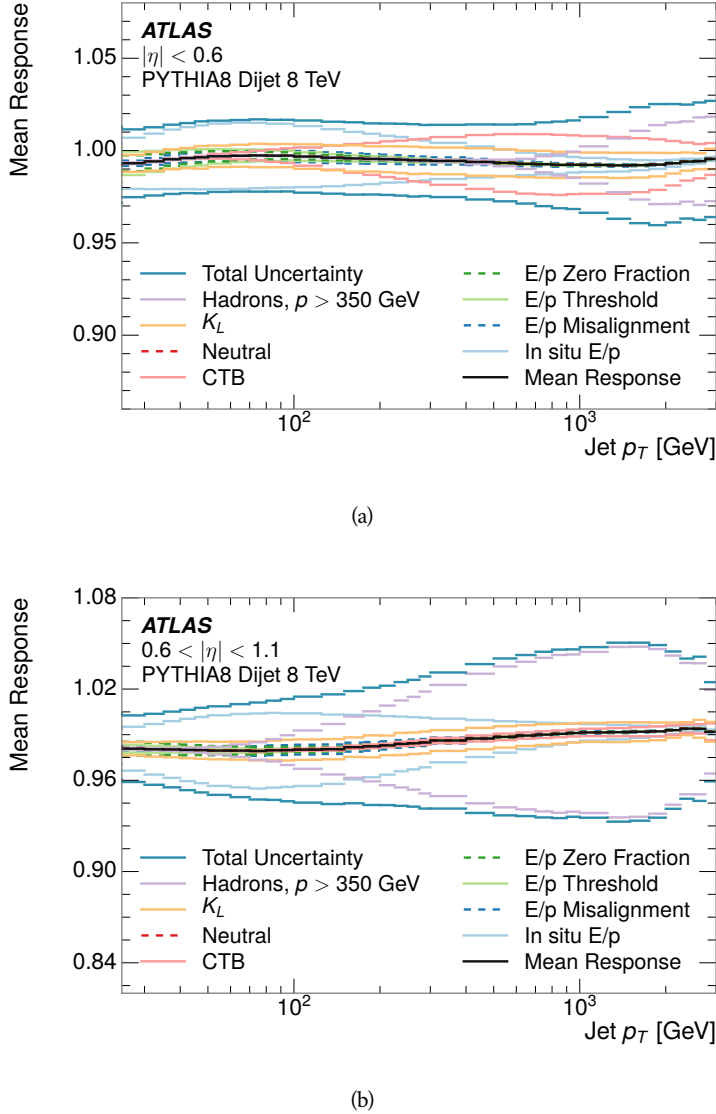


Figure 20: The [JES](#) uncertainty contributions, as well as the total [JES](#) uncertainty, as a function of jet p_T for (a) $|\eta| < 0.6$ and (b) $0.6 < |\eta| < 1.1$.

743 9.3 SUMMARY

744 The technique described above provides a jet energy scale and uncertainty by
 745 building up jet corrections from the energy deposits of constituent particles. The
 746 E/p measurements are crucial in providing corrections for the majority of parti-
 747 cles in the jets. The uncertainty derived this way is between 2 and 5% and is about
 748 twice as large at corresponding momentum than jet balance methods. However
 749 this is the only uncertainty available for very energetic jets using 2012 data and
 750 simulation, and repeating this method with Run 2 data and simulation will be
 751 important in providing an uncertainty for the most energetic jets in 13 TeV col-
 752 lisions.

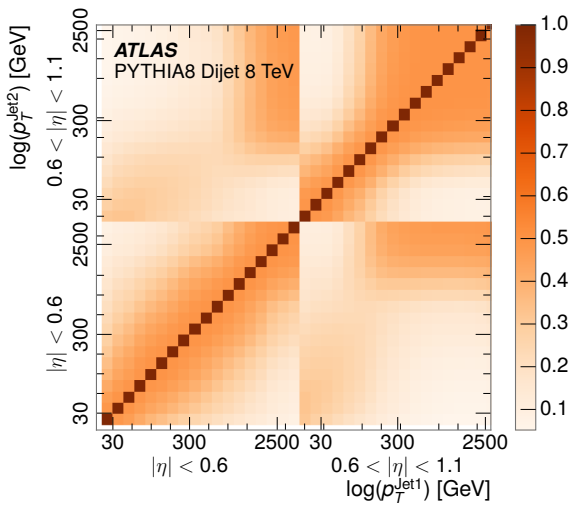


Figure 21: The JES correlations as a function of jet p_T and $|\eta|$ for jets in the central region of the detector.

753

PART V

754

SEARCH FOR LONG-LIVED PARTICLES

755

You can put some informational part preamble text here.

10

756

757 LONG-LIVED PARTICLES IN ATLAS

758 10.1 OVERVIEW AND CHARACTERISTICS

759 10.2 SIMULATION

760

761 EVENT SELECTION

762 11.1 TRIGGER

763 11.2 KINEMATICS AND ISOLATION

764 11.3 STANDARD MODEL REJECTION

765 11.4 IONIZATION

766 11.4.1 DE/DX CALIBRATION

767 11.4.2 MASS ESTIMATION

12

768

769 BACKGROUND ESTIMATION

770 12.1 BACKGROUND SOURCES

771 12.2 PREDICTION METHOD

772 12.3 VALIDATION AND UNCERTAINTY

13

773

774 SYSTEMATIC UNCERTAINTIES AND RESULTS

775 13.1 SYSTEMATIC UNCERTAINTIES

776 13.2 FINAL YIELDS

14

777

778 INTERPRETATION

779 14.1 CROSS SECTIONAL LIMITS

780 14.2 MASS LIMITS

781 14.3 CONTEXT FOR LONG-LIVED SEARCHES

782

PART VI

783

CONCLUSIONS

784

You can put some informational part preamble text here.

15

785

786 SUMMARY AND OUTLOOK

787 15.1 SUMMARY

788 15.2 OUTLOOK

789

PART VII

790

APPENDIX

791

A

792

793 INELASTIC CROSS SECTION

B

794

795 APPENDIX TEST

796 Examples: *Italics*, SMALL CAPS, ALL CAPS ¹. Acronym testing: **UML!** (**UML!**) –
797 **UML! – UML! (UML!) – UML!s**

This appendix is temporary and is here to be used to check the style of the document.

798 B.1 APPENDIX SECTION TEST

799 Random text that should take up a few lines. The purpose is to see how sections
800 and subsections flow with some actual context. Without some body copy be-
801 tween each heading it can be difficult to tell if the weight of the fonts, styles,
802 and sizes use work well together.

803 B.1.1 APPENDIX SUBECTION TEST

804 Random text that should take up a few lines. The purpose is to see how sections
805 and subsections flow with some actual context. Without some body copy be-
806 tween each heading it can be difficult to tell if the weight of the fonts, styles,
807 and sizes use work well together.

808 B.2 A TABLE AND LISTING

809 Curabitur tellus magna, porttitor a, commodo a, commodo in, tortor. Donec in-
810 terdum. Praesent scelerisque. Maecenas posuere sodales odio. Vivamus metus la-
811 cus, varius quis, imperdiet quis, rhoncus a, turpis. Etiam ligula arcu, elementum a,
812 venenatis quis, sollicitudin sed, metus. Donec nunc pede, tincidunt in, venenatis
813 vitae, faucibus vel, nibh. Pellentesque wisi. Nullam malesuada. Morbi ut tellus ut
814 pede tincidunt porta. Lorem ipsum dolor sit amet, consectetur adipiscing elit.
815 Etiam congue neque id dolor.

816 There is also a Python listing below Listing 1.

1 Footnote example.

LABITUR BONORUM PRI NO	QUE VISTA	HUMAN
fastidii ea ius	germano	demonstratea
suscipit instructior	titulo	personas
quaestio philosophia	facto	demonstrated

Table 2: Autem usu id.

817 B.3 SOME FORMULAS

Due to the statistical nature of ionisation energy loss, large fluctuations can occur in the amount of energy deposited by a particle traversing an absorber element². Continuous processes such as multiple scattering and energy loss play a relevant role in the longitudinal and lateral development of electromagnetic and hadronic showers, and in the case of sampling calorimeters the measured resolution can be significantly affected by such fluctuations in their active layers. The description of ionisation fluctuations is characterised by the significance parameter κ , which is proportional to the ratio of mean energy loss to the maximum allowed energy transfer in a single collision with an atomic electron:

You might get unexpected results using math in chapter or section heads.
Consider the pdfspacing option.

$$\kappa = \frac{\xi}{E_{\max}} \quad (1)$$

E_{\max} is the maximum transferable energy in a single collision with an atomic electron.

$$E_{\max} = \frac{2m_e\beta^2\gamma^2}{1 + 2\gamma m_e/m_x + (m_e/m_x)^2},$$

818 where $\gamma = E/m_x$, E is energy and m_x the mass of the incident particle, $\beta^2 =$
 819 $1 - 1/\gamma^2$ and m_e is the electron mass. ξ comes from the Rutherford scattering
 820 cross section and is defined as:

$$\xi = \frac{2\pi z^2 e^4 N_{Av} Z \rho \delta x}{m_e \beta^2 c^2 A} = 153.4 \frac{z^2}{\beta^2} \frac{Z}{A} \rho \delta x \text{ keV},$$

821 where

822 z charge of the incident particle
 823 N_{Av} Avogadro's number
 824 Z atomic number of the material
 825 A atomic weight of the material
 826 ρ density
 δx thickness of the material
 823 κ measures the contribution of the collisions with energy transfer close to
 824 E_{\max} . For a given absorber, κ tends towards large values if δx is large and/or if
 825 β is small. Likewise, κ tends towards zero if δx is small and/or if β approaches
 826 1.

2 Examples taken from Walter Schmidt's great gallery:
<http://home.vrweb.de/~was/mathfonts.html>

Listing 1: A floating example (listings manual)

```
1 for i in xrange(10):
    print i, i*i, i*i*i
print "done"
```

827 The value of κ distinguishes two regimes which occur in the description of
828 ionisation fluctuations:

- 829 1. A large number of collisions involving the loss of all or most of the incident
830 particle energy during the traversal of an absorber.

831 As the total energy transfer is composed of a multitude of small energy
832 losses, we can apply the central limit theorem and describe the fluctua-
833 tions by a Gaussian distribution. This case is applicable to non-relativistic
834 particles and is described by the inequality $\kappa > 10$ (i. e., when the mean
835 energy loss in the absorber is greater than the maximum energy transfer
836 in a single collision).

- 837 2. Particles traversing thin counters and incident electrons under any condi-
838 tions.

839 The relevant inequalities and distributions are $0.01 < \kappa < 10$, Vavilov
840 distribution, and $\kappa < 0.01$, Landau distribution.

841 BIBLIOGRAPHY

- 842 [1] ATLAS Collaboration. “The ATLAS Simulation Infrastructure”. In: *Eur.*
843 *Phys. J. C* 70 (2010), p. 823. doi: [10.1140/epjc/s10052-010-1429-9](https://doi.org/10.1140/epjc/s10052-010-1429-9).
844 arXiv: [1005.4568 \[hep-ex\]](https://arxiv.org/abs/1005.4568). SOFT-2010-01.
- 845 [2] ATLAS Collaboration. “A study of the material in the ATLAS inner de-
846 tector using secondary hadronic interactions”. In: *JINST* 7 (2012), P01013.
847 doi: [10.1088/1748-0221/7/01/P01013](https://doi.org/10.1088/1748-0221/7/01/P01013). arXiv: [1110.6191 \[hep-ex\]](https://arxiv.org/abs/1110.6191).
848 PERF-2011-08.
- 849 [3] ATLAS Collaboration. *Summary of ATLAS Pythia 8 tunes*. ATL-PHYS-PUB-
850 2012-003. 2012. url: <http://cds.cern.ch/record/1474107>.
- 851 [4] ATLAS Collaboration. “Jet energy measurement with the ATLAS detector
852 in proton–proton collisions at $\sqrt{s} = 7$ TeV”. In: *Eur. Phys. J. C* 73 (2013),
853 p. 2304. doi: [10.1140/epjc/s10052-013-2304-2](https://doi.org/10.1140/epjc/s10052-013-2304-2). arXiv: [1112.6426 \[hep-ex\]](https://arxiv.org/abs/1112.6426). PERF-2011-03.
- 855 [5] ATLAS Collaboration. “Single hadron response measurement and calorime-
856 ter jet energy scale uncertainty with the ATLAS detector at the LHC”. In:
857 *Eur. Phys. J. C* 73 (2013), p. 2305. doi: [10.1140/epjc/s10052-013-2305-1](https://doi.org/10.1140/epjc/s10052-013-2305-1). arXiv: [1203.1302 \[hep-ex\]](https://arxiv.org/abs/1203.1302). PERF-2011-05.
- 859 [6] ATLAS Collaboration. “Electron and photon energy calibration with the
860 ATLAS detector using LHC Run 1 data”. In: *Eur. Phys. J. C* 74 (2014), p. 3071.
861 doi: [10.1140/epjc/s10052-014-3071-4](https://doi.org/10.1140/epjc/s10052-014-3071-4). arXiv: [1407.5063 \[hep-ex\]](https://arxiv.org/abs/1407.5063). PERF-2013-05.
- 863 [7] ATLAS Collaboration. “Jet energy measurement and its systematic uncer-
864 tainty in proton–proton collisions at $\sqrt{s} = 7$ TeV with the ATLAS detec-
865 tor”. In: *Eur. Phys. J. C* 75 (2015), p. 17. doi: [10.1140/epjc/s10052-014-3190-y](https://doi.org/10.1140/epjc/s10052-014-3190-y). arXiv: [1406.0076 \[hep-ex\]](https://arxiv.org/abs/1406.0076). PERF-2012-01.
- 867 [8] ATLAS Collaboration. “A measurement of the calorimeter response to sin-
868 ggle hadrons and determination of the jet energy scale uncertainty using
869 LHC Run-1 pp -collision data with the ATLAS detector”. In: (2016). arXiv:
870 [1607.08842 \[hep-ex\]](https://arxiv.org/abs/1607.08842). PERF-2015-05.
- 871 [9] ATLAS Collaboration. “Topological cell clustering in the ATLAS calorime-
872 ters and its performance in LHC Run 1”. In: (2016). arXiv: [1603.02934 \[hep-ex\]](https://arxiv.org/abs/1603.02934).
- 874 [10] E. Abat et al. “Study of energy response and resolution of the ATLAS barrel
875 calorimeter to hadrons of energies from 20 to 350 GeV”. In: *Nucl. Instrum.*
876 *Meth. A* 621.1-3 (2010), pp. 134 – 150. doi: <http://dx.doi.org/10.1016/j.nima.2010.04.054>.

- [11] P. Adragna et al. "Measurement of Pion and Proton Response and Longitudinal Shower Profiles up to 20 Nuclear Interaction Lengths with the ATLAS Tile Calorimeter". In: *Nucl. Instrum. Meth. A* 615 (2010), pp. 158–181. doi: [10.1016/j.nima.2010.01.037](https://doi.org/10.1016/j.nima.2010.01.037).
- [12] S. Agostinelli et al. "GEANT4: A simulation toolkit". In: *Nucl. Instrum. Meth. A* 506 (2003), pp. 250–303. doi: [10.1016/S0168-9002\(03\)01368-8](https://doi.org/10.1016/S0168-9002(03)01368-8).
- [13] N. S. Amelin et al. "Transverse flow and collectivity in ultrarelativistic heavy-ion collisions". In: *Phys. Rev. Lett.* 67 (1991), p. 1523. doi: [10.1103/PhysRevLett.67.1523](https://doi.org/10.1103/PhysRevLett.67.1523).
- [14] N. S. Amelin et al. "Collectivity in ultrarelativistic heavy ion collisions". In: *Nucl. Phys. A* 544 (1992), p. 463. doi: [10.1016/0375-9474\(92\)90598-E](https://doi.org/10.1016/0375-9474(92)90598-E).
- [15] B. Andersson, A. Tai, and B.-H. Sa. "Final state interactions in the (nuclear) FRITIOF string interaction scenario". In: *Z. Phys. C* 70 (1996), pp. 499–506. doi: [10.1007/s002880050127](https://doi.org/10.1007/s002880050127).
- [16] B. Andersson et al. "A model for low-pT hadronic reactions with generalizations to hadron-nucleus and nucleus-nucleus collisions". In: *Nucl. Phys. B* 281 (1987), p. 289. doi: [10.1016/0550-3213\(87\)90257-4](https://doi.org/10.1016/0550-3213(87)90257-4).
- [17] H. W. Bertini and P. Guthrie. "News item results from medium-energy intranuclear-cascade calculation". In: *Nucl. Instr. and Meth. A* 169 (1971), p. 670. doi: [10.1016/0375-9474\(71\)90710-X](https://doi.org/10.1016/0375-9474(71)90710-X).
- [18] L. V. Bravin et al. "Scaling violation of transverse flow in heavy ion collisions at AGS energies". In: *Phys. Lett. B* 344 (1995), p. 49. doi: [10.1016/0370-2693\(94\)01560-Y](https://doi.org/10.1016/0370-2693(94)01560-Y).
- [19] L. V. Bravina et al. "Fluid dynamics and Quark Gluon string model - What we can expect for Au+Au collisions at 11.6 AGeV/c". In: *Nucl. Phys. A* 566 (1994), p. 461. doi: [10.1016/0375-9474\(94\)90669-6](https://doi.org/10.1016/0375-9474(94)90669-6).
- [20] CMS Collaboration. "The CMS barrel calorimeter response to particle beams from 2 to 350 GeV/c". In: *Eur. Phys. J. C* 60.3 (2009). doi: [10.1140/epjc/s10052-009-0959-5](https://doi.org/10.1140/epjc/s10052-009-0959-5).
- [21] H. S. Fesefeldt. *GHEISHA program*. Pitha-85-02, Aachen. 1985.
- [22] G. Folger and J.P. Wellisch. "String parton models in Geant4". In: (2003). arXiv: [nucl-th/0306007](https://arxiv.org/abs/nucl-th/0306007).
- [23] B. Ganhuyag and V. Uzhinsky. "Modified FRITIOF code: Negative charged particle production in high energy nucleus nucleus interactions". In: *Czech. J. Phys.* 47 (1997), pp. 913–918. doi: [10.1023/A:1021296114786](https://doi.org/10.1023/A:1021296114786).
- [24] M. P. Guthrie, R. G. Alsmiller, and H. W. Bertini. "Calculation of the capture of negative pions in light elements and comparison with experiments pertaining to cancer radiotherapy". In: *Nucl. Instrum. Meth.* 66 (1968), pp. 29–36. doi: [10.1016/0029-554X\(68\)90054-2](https://doi.org/10.1016/0029-554X(68)90054-2).
- [25] J. Beringer et al. (Particle Data Group). "Review of Particle Physics". In: *Chin. Phys. C* 38 (2014), p. 090001. URL: <http://pdg.lbl.gov>.

- 920 [26] V.A. Karmanov. "Light Front Wave Function of Relativistic Composite
921 System in Explicitly Solvable Model". In: *Nucl. Phys. B* 166 (1980), p. 378.
922 doi: [10.1016/0550-3213\(80\)90204-7](https://doi.org/10.1016/0550-3213(80)90204-7).
- 923 [27] Hung-Liang Lai, Marco Guzzi, Joey Huston, Zhao Li, Pavel M. Nadolsky,
924 et al. "New parton distributions for collider physics". In: *Phys. Rev. D* 82
925 (2010), p. 074024. doi: [10.1103/PhysRevD.82.074024](https://doi.org/10.1103/PhysRevD.82.074024). arXiv: [1007.2241 \[hep-ph\]](https://arxiv.org/abs/1007.2241).
- 927 [28] A.D. Martin, W.J. Stirling, R.S. Thorne, and G. Watt. "Parton distributions
928 for the LHC". In: *Eur. Phys. J. C* 63 (2009). Figures from the [MSTW Website](#),
929 pp. 189–285. doi: [10.1140/epjc/s10052-009-1072-5](https://doi.org/10.1140/epjc/s10052-009-1072-5). arXiv: [0901.0002](https://arxiv.org/abs/0901.0002).
- 931 [29] B. Nilsson-Almqvist and E. Stenlund. "Interactions Between Hadrons and
932 Nuclei: The Lund Monte Carlo, Fritiof Version 1.6". In: *Comput. Phys. Com-*
933 *mun.* 43 (1987), p. 387. doi: [10.1016/0010-4655\(87\)90056-7](https://doi.org/10.1016/0010-4655(87)90056-7).
- 934 [30] A. Ribon et al. *Status of Geant4 hadronic physics for the simulation of LHC*
935 *experiments at the start of LHC physics program*. CERN-LCGAPP-2010-02.
936 2010. URL: <http://lcgapp.cern.ch/project/docs/noteStatusHadronic2010.pdf>.
- 938 [31] A. Sherstnev and R.S. Thorne. "Parton Distributions for LO Generators".
939 In: *Eur. Phys. J. C* 55 (2008), pp. 553–575. doi: [10.1140/epjc/s10052-008-0610-x](https://doi.org/10.1140/epjc/s10052-008-0610-x). arXiv: [0711.2473](https://arxiv.org/abs/0711.2473).
- 941 [32] T. Sjöstrand, S. Mrenna, and P. Skands. "A Brief Introduction to PYTHIA
942 8.1". In: *Comput. Phys. Commun.* 178 (2008), pp. 852–867. doi: [10.1016/j.cpc.2008.01.036](https://doi.org/10.1016/j.cpc.2008.01.036). arXiv: [0710.3820](https://arxiv.org/abs/0710.3820).
- 944 [33] Peter Speckmayer. "Energy Measurement of Hadrons with the CERN AT-
945 LAS Calorimeter". Presented on 18 Jun 2008. PhD thesis. Vienna: Vienna,
946 Tech. U., 2008. URL: <http://cds.cern.ch/record/1112036>.

₉₄₇ DECLARATION

₉₄₈ Put your declaration here.

₉₄₉ *Berkeley, CA, September 2016*

₉₅₀

Bradley Axen

951

952 COLOPHON

953

Not sure that this is necessary.